Structural response of cold-formed lipped Z purlins – Part 2 numerical modelling and optimisation of lip size

Almatrafi, Meshal; Theofanous, Marios; Dirar, Samir; Bock, Marina

DOI:
10.1016/j.tws.2021.107453

Document Version
Peer reviewed version

Citation for published version (Harvard):
Almatrafi, M, Theofanous, M, Dirar, S & Bock, M 2021, 'Structural response of cold-formed lipped Z purlins – Part 2 numerical modelling and optimisation of lip size', *Thin-Walled Structures*, vol. 161, 107453. https://doi.org/10.1016/j.tws.2021.107453

Structural response of cold-formed lipped Z purlins – Part 2: Numerical modelling and optimisation of lip size

Meshal Almatrafi[1], Marios Theofanous[1*], Samir Dirar[1], Marina Bock[2]

[1] Department of Civil Engineering, University of Birmingham, Edgbaston B15 2TT, UK

[2] School of Architecture and Built Environment, University of Wolverhampton, Wolverhampton, WV1 1LY, UK

[*] Corresponding author, Department of Civil Engineering, University of Birmingham, Edgbaston B15 2TT, UK, Email address: m.theofanous@bham.ac.uk

Abstract

This paper reports a numerical study on the optimization of the lip size of Z-sections under gravity loads. Numerical models of cold-formed steel Z purlins restrained by cladding and angle struts and subjected to sagging moment were developed and validated against a total of 8 experimental results on Z-sections that failed in local or/and distortional buckling reported in the companion paper. Models of varying levels of complexity were generated and the key parameters affecting the structural response were determined by means of a sensitivity analysis. The investigated parameters included the magnitude, shape and combination of initial geometric imperfections pertinent to local and distortional buckling and the simplified or explicit modelling of test details such as struts and sheeting. Having determined the appropriate modelling strategy that leads to the best balance between accuracy and computational cost, parametric studies were conducted to investigate the effect of decreasing or increasing the lip depth on the sections' moment resistance and corresponding failure mode. Based on the parametric study results, the optimal lip size

which maximizes the moment to weight ratio for each section was determined. Finally, all generated FE results are utilized to evaluate the accuracy of the moment resistance prediction of EN 1993-1-3 and the Direct Strength Method.

Keywords

Cold-formed steel, Distortional buckling, Lip size optimisation, FEA, Local buckling, Lipped Z-sections, Purlins.

1. Introduction

In addition to their high strength-to-weight ratio and the ease of installation and transport, cold-formed steel sections are popular in construction due to the flexibility in fabricating complex optimized cross-sectional shapes [1]. Nowadays, many cold-formed producers can customize any cross-section as to better suits the requirements of specific application. Accordingly, finding optimal profiles or sizes of cold-formed steel members, which provide effective and economical solutions, is a topic of great interest [2]. In structural engineering, cross-section optimisation means the minimisation of the used material by reducing the weight while fulfilling strength and serviceability constraints. Generally, cross-section optimization approaches can be categorized into two types, namely shape optimisation and size optimisation [3]. The first aims to find an optimal cross-sectional form with no initial constraints on its shape while the second aims to determine an optimal relative size of the constituent elements within a defined profile. Several studies have been conducted on shape optimisation of cold-formed steel sections employing various mathematical methods and considering different sets of loading conditions and constraints [4-6]. In addition, size optimisation has been also

studied by many researchers to optimise relative dimensions of commonly used cold-formed steel sections such as Z, hat and I-sections [7] and channel beams and columns [8, 9] utilizing techniques such as neural networks and genetic algorithms.

This study builds upon the experimental research on the structural behaviour of lipped Z-section purlins reported in the companion paper [10] and aims to determine the optimal lip size for simply supported laterally restrained purlins subjected to sagging moment, with all other cross-section dimensions remaining constant. Only the bending resistance is considered since the lip size has only a minimal effect on stiffness, whilst it significantly affects the distortional buckling resistance and hence the flexural capacity of Z sections. The objective function that needs be minimised to obtain the optimal lip size is defined herein as the weight-to-flexural strength ratio. To this end a pragmatic approach is followed involving the numerical simulation of Z-sections with different lip sizes and the determination of the moment resistance for each model. Initially an FE model is developed and validated against the experimental results reported in [10]. Thereafter parametric studies are conducted investigating the effect of increasing and decreasing the lip size on the sections' flexural resistance. Based on the obtained results an optimal lip size is determined for each Z-section modelled. Finally, all numerical results are utilized to assess accuracy of the predictions of European [11, 12] and American design codes [13].

2. Numerical modelling

The finite element software ABAQUS [14] was utilized to generate the numerical models that simulate the response of Z purlins subjected to sagging moment. In all numerical models, geometric imperfections and material non-linearity were employed to obtain a

realistic estimation of the flexural strength. It is noted that the failure modes considered in the FE simulations include local and distortional buckling only in accordance with the experimental results [10] against which the FE models were validated. All FE models have a clear span length of 3 meters, whilst four point load were applied at fifth points of the beams to approximate a uniformly distributed load in accordance with the tests [10]. Details on the modelling assumptions are given in the following sections.

2.1 Element type and discretization

The linear 4-nodded shell element S4R with reduced integration was used to discretise the modelled purlins as it was shown to perform well in similar studies [15-18]. To obtain a good balance between accuracy and computational cost, a mesh convergence study was conducted on a typical purlin by running successive analyses with increasingly finer meshes and plotting the obtained strength against the number of elements. In all models the assumptions reported in the following sections were employed and only the mesh size was varied, whilst keeping the aspect ratio of the elements close to unity. A mesh convergence study involving six different mesh sizes namely 30, 25, 20, 15, 12 and 10 mm was carried out. Fig. 1 summarises the results of the mesh convergence study for a typical purlin where it can be clearly observed that decreasing the mesh has a marked influence of the obtained results until a mesh size of 12x12, whereafter the results do not change significantly. Therefore, a uniform mesh size of 12x12 is employed for the flat plated parts of all models, whilst 3 elements were used to discretise the curved corner regions and 3 elements were used over the flat lip depth. A typical meshed model with a mesh size of 12x12 is shown in Fig. 2. The same discretization was employed in the parametric studies.

2.2 Initial geometric imperfections

Geometric imperfections are defined as deviations of a member actual geometry from its nominal one. The magnitude and combination of initial geometric imperfections have a significant impact on section capacity and structural response; therefore, they need to be included carefully in the models. Since this paper studies the behaviour of laterally restrained purlins and given that all specimens failed by local or distortional buckling, only initial geometric imperfections pertinent to local and distortional buckling mode shapes were considered.

In the companion paper [15], based on the results of which the FE models are validated herein, no geometric imperfection measurements were reported. This was due to the tests having been performed on twin purlin specimens assembled from individual purlins connected to each other via angle struts and restrained at the top by profiled sheeting. The assembly process introduced additional geometric imperfections or eliminated preexisting ones in individual purlins as discussed in the companion paper. Therefore, in this study, the initial geometric imperfections were treated as a modelling convenience to trigger buckling and failure in the desired mode, rather than as a physical reality [17]. To this end a linear eigenvalue buckling analysis was initially conducted and the buckling mode shapes corresponding to the lowest critical stress pertinent to local buckling (i.e. short halfwave length) and distortional buckling (long halfwave length) were utilized to perturb the initial geometry and trigger buckling. Fig. 3 shows typical mode shapes for local and distortional buckling extracted from eigenvalue analysis.

Three different values for the magnitudes of the imperfections corresponding to local and distortional buckling were considered as summarised in Table 1. The imperfection

magnitude values stated as fractions of the section thickness for cases a and b were obtained from statistical data for lipped channel sections reported by Zeinoddini and Schafer [19] and correspond to the 50% and 75% percentile of the cumulative distribution function of measured geometric imperfections for local and distortional buckling. Case c utilises a Dawson and Walker [20] type of equation to estimate the magnitude of the geometric imperfection for distortional buckling, assuming that the magnitude depends on the cross-section slenderness, whilst for the local buckling imperfection amplitude, the value h/200 recommended in Annex C of EN 1993-1-5 [12] has been adopted herein, where h is the overall depth of the section. The critical buckling stress for distortional buckling, which is required to determine the imperfection amplitude for the distortional buckling mode shape, was determined using the software CUFSM [21].

The initial geometric imperfection f_0 applied to each model was simulated as a linear combination of the imperfections for local and distortional buckling in accordance with Equation (1), where α_i is the magnitude for each mode predicted by the 3 amplitudes considered from Table 1, C_i is a coefficient that controls the sign and portion of the amplitude and $\emptyset_i$ is the mode shape [19].

$$f_0 = \sum_i \alpha_i C_i \emptyset_i \qquad i = number\ of\ \text{mode shape} \tag{1}$$

A thorough explanation of numerical imperfections modelling strategies can be found in [19]. As summarised in [19], there are two classical approaches to determine C_i, namely the circle-SRSS (square root of the sum of squares) and the square-max. A graphical representation of these methods is shown in Fig. 4, where C_L and C_d are the coefficients for imperfections corresponding to local and distortional buckling, respectively. In the square-max approach, the maximum magnitude for every mode with different signs is

considered, while in the SRSS, the relationship between the amplitudes of the two mode shapes is defined by Equation (2).

$$\sqrt{{C_L}^2 + {C_D}^2} = 1 \quad (2)$$

The numbered points in Fig. 4 define various possible combinations of the two buckling mode shapes. These include combinations 1-4 according to the square-max method and combinations 5-8 following the SRSS method. It has to be noted that only cases 1, 2, 5, 6 are considered in this analysis because, as observed in the tests [10], distortional buckling occurred only in the opening mode (i.e. outwards) hence considering cases with a negative sign (closing mode) would not accurately capture the observed failure modes. For each specimen, twelve analyses were carried out (i.e. 3 imperfection magnitudes and 4 combinations of imperfections) in order to obtain the magnitude and combination of imperfections that leads to the best agreement with the test experimental results. This is discussed later in the validation section of this paper.

2.3 Materials properties, residual stresses and corner strength enhancements

The experimental results from tensile coupon tests extracted from the flange of sections cut from the same member length as that used for the tested sections are reported in the companion paper [10]. All sections had a nominal yield strength of 450 MPa, with the experimentally determined one being 466 MPa on average. Young's modulus was 200000 MPa on average with very small variations. Some of the material coupons exhibited gradual yielding, whilst most stress-strain curves displayed a well-defined yield plateau followed by strain-hardening. In the numerical analyses reported herein the

experimentally derived material response was adopted for the validation of the models. The two stage Ramberg Osgood material model originally proposed in [22] and modified in [23] as given in Equations (3) and (4) for the 1st and 2nd stage, respectively, was used to simulate the nonlinear material behaviour.

$$\varepsilon = \frac{\sigma}{E} + 0.002\,(\sigma/\sigma_{0.2})^{n} \qquad \text{For } \sigma \leq \sigma_{0.2} \tag{3}$$

$$\varepsilon = \frac{(\sigma-\sigma_{0.2})}{E_{0.2}} + \left(\varepsilon t_{1.0} - \varepsilon t_{0.2} - \frac{\sigma_{1.0}-\sigma_{0.2}}{E_{0.2}}\right) \times \left(\frac{\sigma-\sigma_{0.2}}{\sigma_{1.0}-\sigma_{0.2}}\right)^{n_{0.2,1.0}} + \varepsilon t_{0.2} \quad \text{For } \sigma > \sigma_{0.2} \tag{4}$$

In these equations, n is the non-linear parameter exponent of the classical Ramberg-Osgood model and ranged between 17 and 20 for the material reported in [10], E is the Young's modulus, $\sigma_{0.2}$ is the proof stress corresponding to 0.2 % plastic strain, $\sigma_{1.0}$ is the proof stress corresponding to 1 % plastic strain, $E_{0.2}$ is the tangent modulus at 0.2% proof stress, $E_{0.2} = \frac{E}{1+0.002\mathrm{n}\frac{E}{\sigma_{0.2}}}$, $\varepsilon t_{0.2}$ is the total strain at the 0.2% proof stress $\varepsilon t_{0.2} = 0.002 + \sigma_{0.2}/E$, $\varepsilon t_{1.0}$ is the total strain at the 1% proof stress $\varepsilon t_{1.0} = 0.01 + \sigma_{1.0}/E$, and $n_{0.2,1.0}$ is a strain hardening coefficient for a curve that passes through $\sigma_{0.2}$ and $\sigma_{1.0}$. The value of $n_{0.2,1.0}$ ranges from 0.9 to 2 for the material reported in [10]. As later observed, the effect of material modelling on the numerical results was not significant due to the high slenderness of the simulated sections.

The engineering stress-strain curves defined by Equations (3) and (4) namely σ_{nom} and ε_{nom} were converted into true stress σ_{true} and logarithmic plastic strain $\varepsilon_{pl,true}$ as required by ABAQUS according to Equations (5) and (6).

$$\sigma_{true} = \sigma_{nom}\,(1 + \varepsilon_{nom}) \tag{5}$$

$$\varepsilon_{pl,true} = ln(1 + \varepsilon_{nom}) - \sigma_{nom}/E \quad (6)$$

It is well known that the cold-forming process introduces both bending residual stresses [24] and strength enhancements in the corner regions of the cold-formed sections. The bending residual stresses lead to an earlier loss of stiffness under applied load hence promoting buckling, whilst the corner strength enhancements increase the cross-sectional strength as the press-braked corners possess higher strength than the flat material of the section. Since the material coupons curved upon their extraction from the section due to the release of bending residual stresses, the effect of the residual stresses is reflected in the obtained material properties, as the residual stresses are reintroduced as the coupons were straightened during the initial stages of tensile testing. Therefore, the effect of residual stresses is not explicitly considered in the models. Given that strength enhancements and residual stresses are caused by the same process, in line with [16], neither the strength enhancements of the corner regions nor the bending residual stresses have been explicitly modelled.

2.4 Modelling of structural details

Boundary conditions significantly affect the structural response of the FE models, hence they need to accurately reflect the actual support conditions employed in practice. The tests that are simulated herein, employed twin purlins connected to one another via angle struts as discussed in the companion paper [10] and shown in Figure 4.5. Given the importance of the restrain provided by the sheeting and the angle struts to the purlins, their effect needs to be incorporated in the FE models. The most accurate but also computationally expensive approach is to explicitly model the sheeting and angle struts

with shell elements and account for the contact between sheeting and purlins, whereas a computationally less expensive simplification would be to replace the sheeting and angle struts with relevant support conditions, i.e. restraining the purlin against out of plane deflections at the locations where it is connected to angle struts and sheeting. In between these two extremes are the options involving explicit modelling of only the sheeting or the angle struts with the effect of the other simulated as boundary conditions, as outlined in Table 2, where four modelling approaches of varying complexity are summarised and assessed with respect to their computational cost and complexity. The corresponding geometry of the FE models is shown in Fig. 6. For all cases, to increase computational efficiency, the symmetry with respect to boundary conditions, loading and observed failure mode was exploited and only one of the twin purlins was modelled with suitable boundary conditions simulating the effect of the presence of the twin purlin. In all models the loads were applied as equal point loads on the flange whilst the support reactions, were applied on the end sections which were constrained to remain rigid via kinematic coupling, thus reflecting the presence of the angle cleat shown in Fig. 5.

The boundary conditions employed for the simplified model (model i) are shown in Fig. 7, where the z-axis (DOF 3) corresponds to the longitudinal member axis, the y-axis (DOF 2) is parallel to the web and the x-axis (DOF 1) is parallel to the flange. For models (ii) and (iv), where the struts are explicitly modelled, tie constrains were used to model the connection of the struts to the purlin. To model the contact between the cladding (for model ii , iii) and the compression flange of the beam, general contact with hard behaviour in the normal direction and frictionless behaviour in the tangential direction was assumed. The differences between the four models outlined in Table 2 are discussed hereafter.

3. Validation

The accuracy of the four modelling strategies employed to simulate the effect of struts and cladding on the structural response of the modelled purlins is assessed by comparing the resulting behaviour against obtained tests results [10]. The difference between the four models is quantified in Table 3 in terms of moment resistance, where all 8 specimens have been modelled following the four modelling strategies discussed previously, whilst the effect of the adopted modelling strategy on the overall structural response is demonstrated in Fig. 8 for purlin Z24620. In Table 3, where M_{FE} and M_T are the obtained maximum moment from numerical models and tests respectively, an excellent agreement with the experimental results is observed for all modelling strategies considered, with model (iii) displaying the best strength predictions on average and model (iv) the lowest scatter. However, the marginal improvement in accuracy when the struts and/or cladding are explicitly modelled is outweighed by the significant increase in computational cost. Furthermore, the focus of this study is the behaviour of the purlin sections rather than the effect of structural details, hence the simplified modelling approach (i) will be employed in the remainder of the paper.

To investigate the effect of the initial imperfections on the numerical flexural strength and select the most appropriate imperfection amplitudes and combinations of local and distortional buckling mode shapes, the numerically obtained results are compared against the experimental results for all combinations of initial geometric imperfections considered, as reported in Table 4. The numbers 1, 2, 5 and 6 in Table 4 correspond to the type of combination employed for the local and distortional buckling imperfections as shown in Fig. 4, whereas the letter a , b and c correspond to the imperfection amplitudes reported in Table 1. All obtained results are based on the simplified modelling strategy (i). Overall, the FE results can accurately capture the experimentally observed failure

modes, as shown in Fig. 9, where the experimental and numerical failure modes of purlins Z14620, Z20620 and Z17625 are depicted. In all cases the observed failure modes, including distortional and local buckling are accurately predicted by the FE models.

For completeness, and to highlight the importance of incorporating initial geometric imperfections pertinent to both local and distortional buckling, the numerical over experimental flexural strength for the purlins considered is reported in Table 5, where the obtained results are based on employing only one buckling mode shape, pertinent to either local or distortional buckling. The utilized amplitudes are the ones reported in Table 1 as amplitudes (c). It can be clearly seen that employing only one buckling mode shape that considering a pure imperfection mode, whether local or distortional, will lead to higher predictions and increased scatter for the moment resistances and overall a worse agreement with the experimental results is obtained compared to using mode shapes representative of both local and distortional buckling.

The imperfections (b) and (c) (see Table 1) following the combinations 1 and 2 provide a better agreement with the experimental results compared to combinations 5 and 6, which display a higher predicted moment resistance and increased scatter. Based on the obtained results, combination 2 of the initial geometric imperfections with amplitudes (c) as shown in Table 1, is deemed suitable and is adopted hereafter in the parametric studies. The average ratio of numerical over experimental moment resistance for all 8 tests is 1.01 with a coefficient of variation (COV) of 0.05.

4. Parametric studies

Having determined the optimal modelling strategy to account for the effect of geometric imperfections and the effect of sheeting and struts at modest computational cost,

parametric studies were carried out to study the effect of decreasing or increasing the lip depth on the sections' moment resistance, assess existing design standards and ultimately optimize the cross-section's lip depth.

The cross-section geometries considered in the parametric studies are reported in Table 6 and include seven nominal section depths ranging from 146 mm to 307 mm. Each of the seven section depths is hereafter referred to with the nominal depth in mm following the letter Z and includes a family of sections with similar midline dimensions but different thicknesses. A range of thicknesses was considered to cover a wide range of cross-section slendernesses, whilst the flange width was 62.5 mm except for the deeper section size of 307 mm for which a flange width of 75 mm was employed in line with [25]. Six lip depths namely 15 mm, 17.5 mm, 20mm, 25 mm, 30 mm and 35 mm were taken into consideration. It should be noted that all section depths considered currently have a nominal lip size of 20 mm [25]. For some of the deeper sections further analysis with deeper lip sizes was conducted to assure that the most efficient cross-section is obtained. It should be noted that all the lip sizes employed in the numerical analysis are within the limits specified in EC3 [11] for the allowable lip size over flange width ratio ($i.e. 0.2 \leq d/b \leq 0.6$). Rounded corners with an internal radius of 4 mm were adopted for all sections in agreement with the average values measured in [10]. The beam length for all sections was fixed at 3 m, thereby resulting in a span to depth ratio ranging from 10 to 21. In agreement with the experimental study [10], four-point loads were applied at a distance of 600 mm from one another and from the supports. Neither corner strength enhancements nor residuals tresses were explicitly considered in the parametric studies, whilst the initial imperfection amplitudes (c) of Table 1 combined according to combination 2 shown in Fig. 4 was adopted as previously discussed.

To account for the two distinct types of material behaviour obtained from material coupon testing [10], two material models were considered, since some coupon test results displayed a yield plateau and others did not. The first material model employs an elastic perfectly plastic stress-strain relationship (EPP) with a yield strength equal to 450 MPa. The second material model considered was a two stage Ramberg-Osgood (R-O) material equation parameters of which are given in Table 6. For both material models, the Young's modulus was assumed equal to 200 GPa in line with the material coupon test results and the Poisson's ratio was taken equal to 0.3. The effect of the adopted material model on the obtained failure mode is shown in Fig. 10, for two typical purlins, where the EPP material can be seen to lead to well defined plastic zones, whilst the effect of strain hardening of the R-O material leads to a more gradual yielding in regions with high stress concentrations.

For each material model assumed, 295 geometric configurations were modelled, hence the parametric study consists of 590 FE simulations. The obtained results are utilised hereafter to determine the optimal lip size for each modelled Z-section and to assess the accuracy of EN 1993-1-3 [11], EN 1993-1-5 [12] as well as the Direct strength method (DSM) [13].

5. Results and discussion

For all sections considered in the parametric study, the moment resistance M_{FE} was extracted and normalised by the weight of the modelled section per meter length W to quantify the effect of increasing the lip size on both strength and weight and obtain the optimal lip size that maximises the strength-to-weight ratio for each section depth

considered. It is noted that the current lip size for all section depths considered herein is 20 mm [25].

For each group of cross-sections with the same depth, the M_{FE}/W ratio is plotted against the lip depth and presented in Fig. 11. Hence Fig. 11 includes 14 graphs, 1 for each nominal section depth considered and each of the 2 material properties assumed (i.e. EPP and R-O). The lip size for which a peak of the M_{FE}/W ratio occurs corresponds to the optimal lip size for the studied sections. As expected, all models assuming an elastic perfectly plastic (EPP) material response reach higher moment resistances compared to identical sections with a rounded material response, as they maintain their stiffness until the yield strength is reached, whilst employing a Ramberg-Osgood (R-O) type of response leads to loss of stiffness at lower stresses and hence cross-sectional instabilities occur earlier. In all cases considered herein the difference in terms of moment resistance between EPP and R-O is less than between 1% and 3% for the geometrically identical sections with the higher end of the range corresponding to less slender sections. For the shallowest of the sections considered (i.e. Z146), increased efficiency can be achieved by increasing the lip size, since no maximum can be observed in Figs. 11(a) and (b). In all other cases, as shown in Fig.11 a clearly defined maximum can be observed for the thinner and most of the thickest sections, which corresponds to either the current lip size of 20 mm or to larger lip sizes. In general, the optimal lip depth increases with increasing section thickness as can be clearly seen in Fig. 11 where the maximum of the M_{FE}/W ratio shifts to the right for thicker sections of the same depth. Hence increased efficiency can be achieved, if the lip size for the same nominal section depth is changed according to the section thickness, however this would be outside current practice and potentially highly impractical.

A summary of the results shown in Fig.11 is reported in Table 7 where all sections considered have been grouped in seven groups according to their nominal depth and the average moment-to-weight ratio within each group is considered. To facilitate a direct comparison of the efficiency of cross-sections employing different lip sizes but which are otherwise geometrically identical, the M_{FE}/W of the all models with a lip size other than the currently employed one has been normalized by the respective ratio of the sections with a lip size of 20 mm. Values of this ratio higher than unity imply that the section is more efficient, whilst values smaller than one correspond to less economical section performance. The optimal lip size for each section depth considered (with all sections with varying thicknesses averaged) is denoted with bold italic font. For all sections, lip sizes below 20 mm lead to decreased efficiency by as much as 7% or 8% for R-O and EPP material respectively, whilst increasing it leads to improved efficiencies particularly for deeper sections, for which gains in the region of 5% can be achieved.

Finally, the performance of the design provisions for bending and local buckling design given in the parts of the European code EN 1993-1-3 and the EN 1993-1-5 (labelled as EC3) [11,12] as well as the DSM [13] method from the American standard AISI is assessed. The predicted moment capacities M_{pred} determined by both design approaches are compared with the moment capacities obtained from the FE analysis M_{FE}. The comparison is shown in Table 8 in terms of the average value of the M_{pred}/M_{FE} ratio of the various cross-sectional thickness taken into consideration within each cross-section range whilst highlighting the material type. A graphical representation is also provided in Fig. 12 where the M_{pred}/M_{FE} ratio is plotted against the non-dimensional slenderness for distortional buckling $\lambda_d$determined as given by Equation (7), where σ_y is the material yield strength (or equivalent 0.2% proof strength for R-O material) and σ_{crd} is the distortional buckling critical strength which has been determined with the CUFSM [21]

$$\lambda_d = (\sigma_y/\sigma_{crd})^{0.5} \quad (7)$$

Overall, both design approaches are observed to be safe though the EC3 predictions are overly conservative underestimating the cross-sectional bending capacity by 10% for the R-O material and raising the level of conservativeness up to 15% when material strain hardening is not considered (i.e. EPP material). The EC3 predictions also show a reasonable scatter with COV values of 6 and 7% for the RO and the EPP material, respectively. In comparison, the DSM reduces the conservatism by 5% with less scattered predictions and therefore is deemed more efficient and reliable than EC3 for all the geometric configurations considered and regardless of material model.

The same observations are depicted in Fig. 12 where it can also be seen that for λ_d values less than 0.9, both design approaches yield results of very similar accuracy but the EC3 approach appears to be less accurate with increasing λ_d, whereas the DSM appears qually consistent and accurate throughout the slenderness range considered.

6. Conclusions

The development of an FE model for the simulation of Z-section purlins failing by local and /or distortional buckling has been reported in this paper. Particular attention was paid to the modelling strategy for considering the effect of structural details such as angle struts and cladding on the structural response of the purlins, whilst a systematic study was carried out to study the effect of initial geometric imperfections and select the most suitable amplitudes and combinations thereof. Upon validation of the results, a parametric study was conducted to study the effect of the lip size on the flexural resistance of the

studied sections. It was determined that all sections, would be less efficient if their current nominal lip size of 20 mm was decreased, whilst some of them would benefit from an increase of their nominal lip size.

The recommendations offer on average material savings of about 6% for the deeper sections and 4% for shallow sections, thus increasing the efficiency of the manufactured purlins. It is noted that the obtained increase in efficiency when the optimal lip size is used, is based on the assumption that no lateral torsional buckling occurs, which, if present, is expected to reduce the effect of the lip size. This matter will be addressed in future studies. Finally, all generated numerical results were utilized to assess the accuracy of European [11, 12] and American [13] design predictions. In all cases, the Direct Strength Method [13] leads to a moderate increase in the predicted strength compared to the European design approach [11, 12], whilst the scatter of the predictions also decreases.

Acknowledgements

The supply of specimens and financial support from Albion Sections Ltd is gratefully acknowledged. The first author would like to thank the Saudi Arabian Cultural Bureau and Umm Al Qura University for sponsoring his doctoral studies.

References

[1] Yu C., Schafer B.W. (2006). Distortional buckling tests on cold-formed steel beams, Journal of Structural Engineering 132(4), 515-528.

[2] Leng J., Guest J.K., Schafer B.W. (2011). Shape optimization of cold-formed steel columns, Thin-Walled Structures 49 (12), 1492-1503.

[3] Ye, J.; Hajirasouliha, I.; Becque, J.; Eslami, A. (2016) Optimum design of cold-formed steel beams using Particle Swarm Optimisation method, Journal of Constructional Steel Research 122, 80-93.

[4] Liu H., Igusa T., Schafer, B.W. (2004). Knowledge-based global optimization of cold-formed steel columns, Thin-Walled Structures 42, 785-801.

[5] Moharrami M., Louhghalam A., Tootkaboni M. (2014). Optimal folding of cold formed steel cross sections under compression, Thin-Walled Structures 76, 145-156.

[6] Leng J.Z., Li Z.J., Guest J.K., Schafer B.W. (2014). Shape optimization of cold-formed steel columns with fabrication and geometric end-use constraints, Thin-Walled Structures 85, 271-290.

[7] Adeli H., Karim A. (1997). Neural network model for optimization of cold-formed steel beams, Journal of Structural Engineering 123, 1535-1543.

[8] Lee J., Kim S.M., Park H.S., Woo B.H. (2005). Optimum design of cold-formed steel channel beams using micro-genetic algorithm, Engineering Structures, 27, 17-24.

[9] Lee J., Kim S.M., Park H.S. (2006). Optimum design of cold-formed steel columns by using micro genetic algorithms, Thin-Walled Structures 44, 952-960.

[10] Almatrafi M., Theofanous M., Dirar S., Gkantou M. Structural response of cold-formed lipped Z purlins – Part 1: Experimental investigation. Thin-Walled Structures. (submitted).

[11] CEN. Eurocode 3: Design of steel structures, Part 1.3: General rules-supplementary rules for cold formed members and sheeting. Brussels, European Committee for Standardization, 2005.

[12] CEN. Eurocode 3: Design of steel structures, Part 1.5: Plated structural elements. Brussels, European Committee for Standardization, 2005.

[13] AISI. North American Specification. Appendix 1: Design of cold-formed steel structural members using the Direct Strength Method. 2004 supplement to the north American specification for the design of cold-formed steel structures, American Iron and Steel Institute, Washington (DC), 2004.

[14] Hibbitt, Karlsson, and Sorensen Inc. ABAQUS, ABAQUS/Standard user's manual volume I–III and ABAQUS CAE manual. Version 6.10, Pawtucket, USA, 2010.

[15] Kyvelou, P.; Gardner, L.; Nethercot, D.A. (2018) Finite element modelling of composite cold-formed steel flooring systems, Engineering Structures 158, 28-42.

[16] Wang, J.; Afshan, S.; Gkantou, M.; Theofanous, M.; Baniotopoulos, C.; Gardner, L. (2016) Flexural behaviour of hot-finished high strength steel square and rectangular hollow sections, Journal of Constructional Steel Research 121, 97-109.

[17] Schafer, B.W.; Li, Z.; Moen, C.D. (2010) Computational modelling of cold-formed steel, Thin-Walled Structures 48, 752-762.

[18] Haidarali M.R., Nethercot D.A. Finite element modelling of cold-formed steel beams under local buckling or combined local/distortional buckling. Thin-Walled Structures, 49, 1554–1562, 2011.

[19] Zeinoddini, V.M.; Schafer, B.W. (2012) Simulation of geometric imperfections in cold-formed steel members using spectral representation approach, Thin-Walled Structures 60, 105–117.

[20] Dawson, R.G.; Walker, A.C. (1972) Post-buckling of geometrically imperfect plates, Journal of the Structural Division 98, 75-94.

[21] Li, Z., Schafer, B.W. Buckling analysis of cold-formed steel members with general boundary conditions using CUFSM: Conventional and constrained finite strip methods", 20th International Specialty Conference on Cold-Formed Steel Structures – Recent Research and Developments in Cold-Formed Steel Design and Construction, pp. 17. 2010.

[22] Mirambell, E., Real, E. (2000). On the calculation of deflections in structural stainless steel beams: an experimental and numerical investigation. Journal of Constructional Steel Research 54(1), 109-133.

[23] Gardner L., Nethercot D.A. (2004). Experiments on stainless steel hollow sections—Part 1: Material and cross-sectional behaviour. Journal of Constructional Steel Research 60(9), 1291-1318.

[24] Schafer B.W., Peköz T. (1998) Computational modeling of cold-formed steel: characterizing geometric imperfections and residual stresses, Journal of Constructional Steel Research 47(3), 193-210.

[25] Albion Sections. Z-purlin, cladding rail and Eaves beams technical manual. (2019). Albion sections [Accessed at: http://albionsections.co.uk/doc/52.pdf].

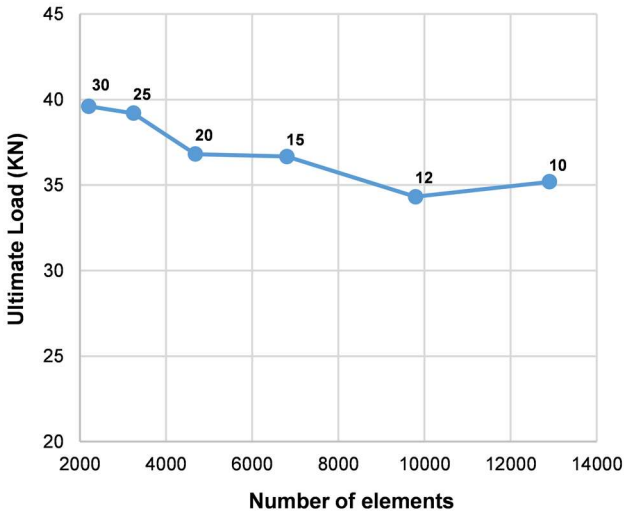

Fig. 1. Mesh convergence study.

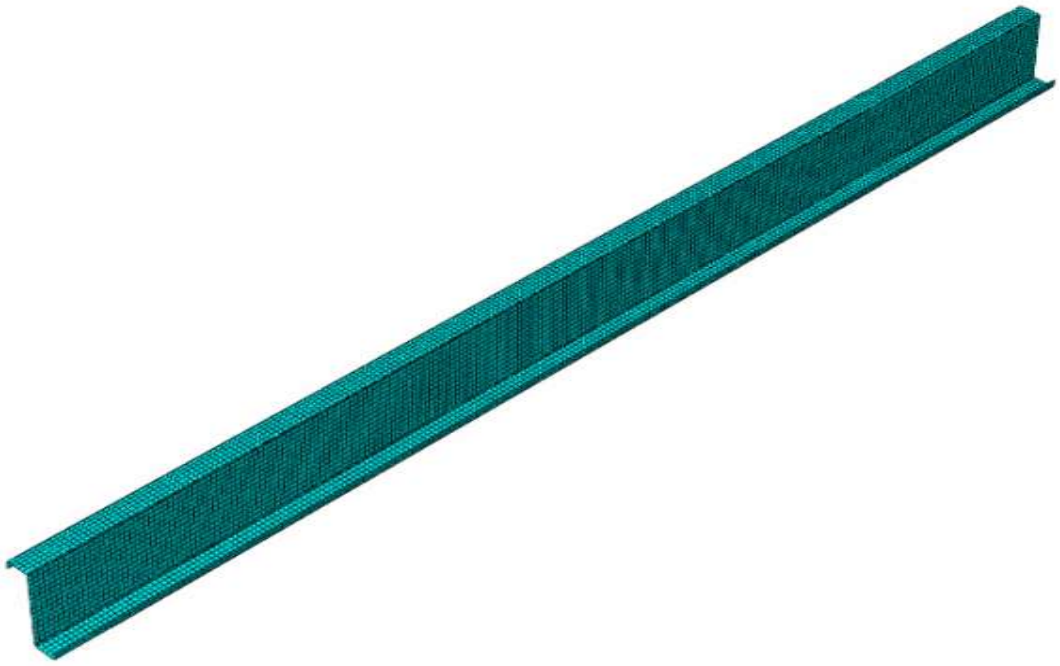

Fig. 2. Discretised FE model of a purlin.

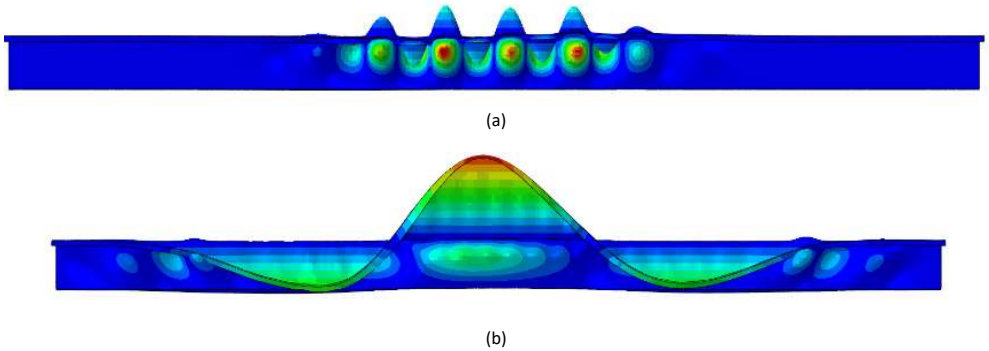

Fig. 3. Typical buckling mode shapes for (a) local and (b) distortional buckling.

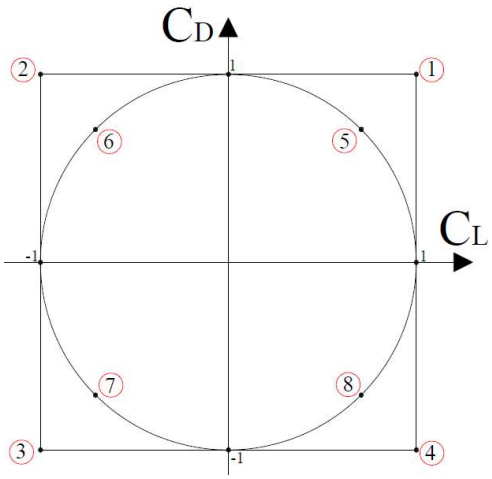

Fig. 4. Square-max and SRSS combinations of initial geometric imperfection amplitudes.

Fig. 5. Detail of the angle struts (left) and sheeting and angle cleat (right).

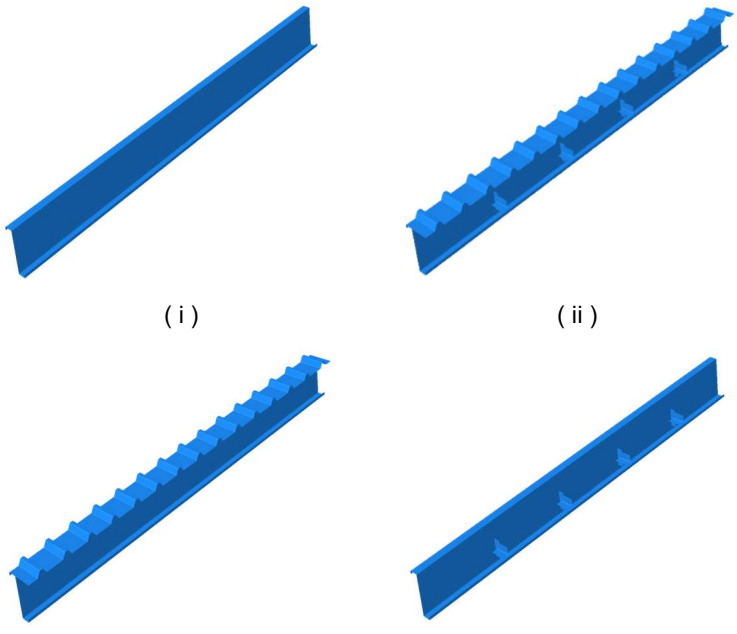

Fig. 6. Four different modelling strategies with varying complexity corresponding to Table 2.

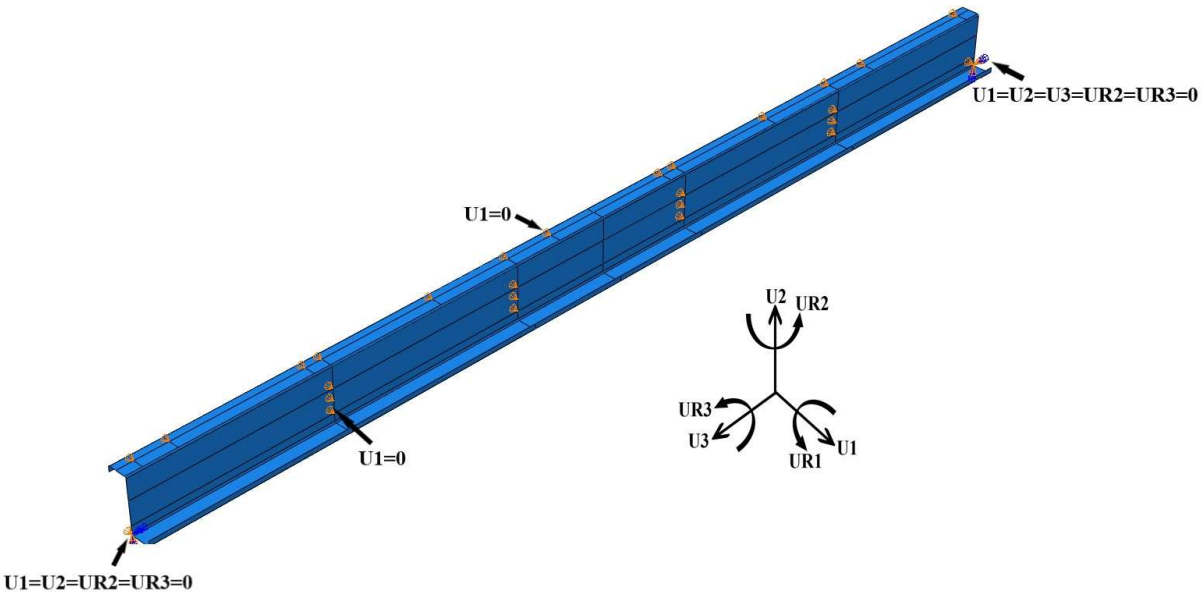

Fig. 7. Boundary conditions.

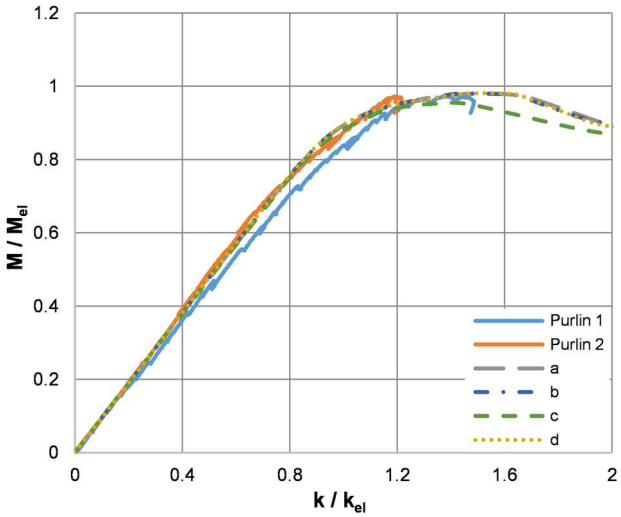

Fig. 8. Effect of modelling approach on the moment-curvature response of purlin Z24620.

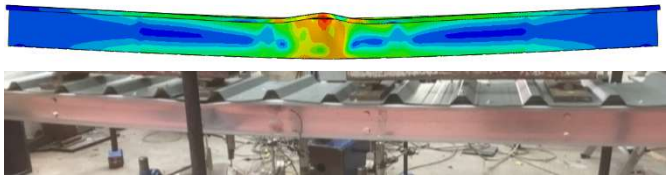

(a) Z14620

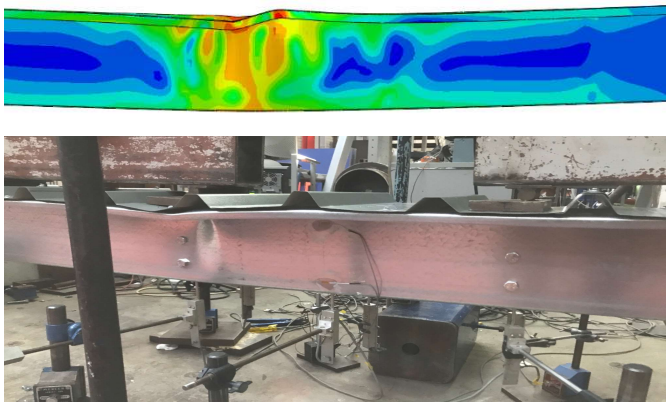

(b) Z20620

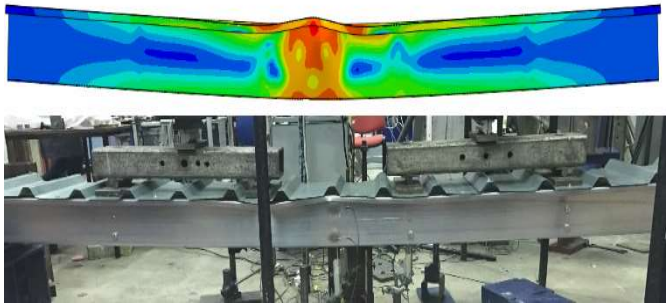

(c) Z17625

Fig. 9. Experimental and numerical failure modes for typical purlins.

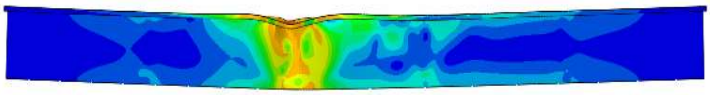

(a)

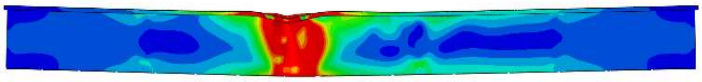

(b)
Z24623

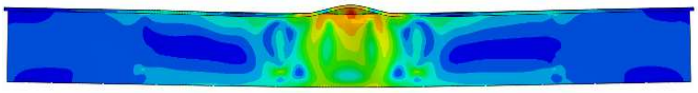

(a)

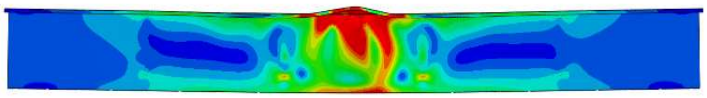

(b)
Z30720

Fig. 10. Comparison between the failure modes of (a) R-O material and (b) EPP material.

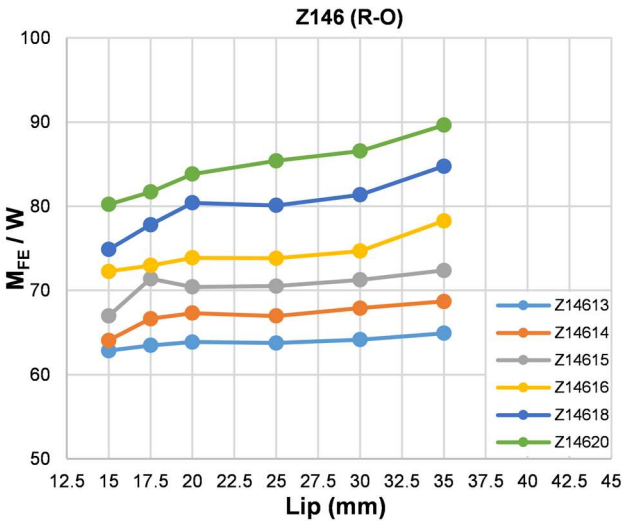
Z146 (R-O)
100
90
80
70
60
50
M_{FE} / W
12.5 15 17.5 20 22.5 25 27.5 30 32.5 35 37.5 40 42.5 45
Lip (mm)
Z14613
Z14614
Z14615
Z14616
Z14618
Z14620

(a)

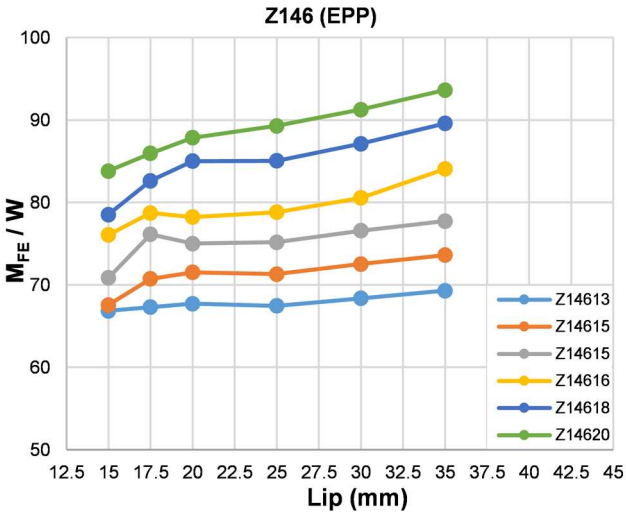
Z146 (EPP)
100
90
80
70
60
50
M_{FE} / W
12.5 15 17.5 20 22.5 25 27.5 30 32.5 35 37.5 40 42.5 45
Lip (mm)
Z14613
Z14615
Z14615
Z14616
Z14618
Z14620

(b)

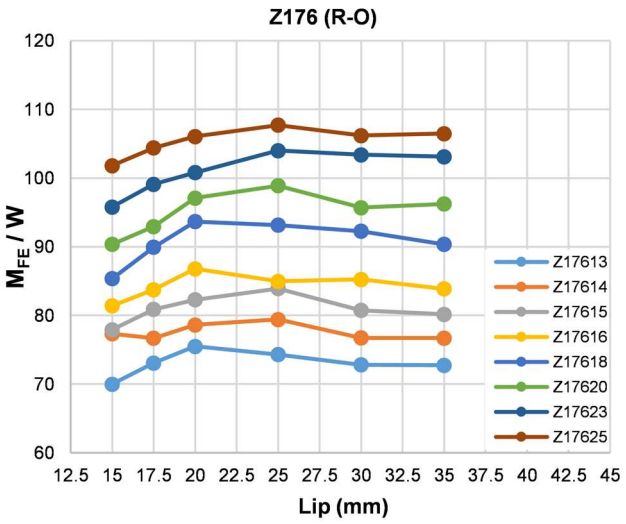
Z176 (R-O)
120
110
100
90
80
70
60
M_{FE} / W
12.5 15 17.5 20 22.5 25 27.5 30 32.5 35 37.5 40 42.5 45
Lip (mm)
Z17613
Z17614
Z17615
Z17616
Z17618
Z17620
Z17623
Z17625

(c)

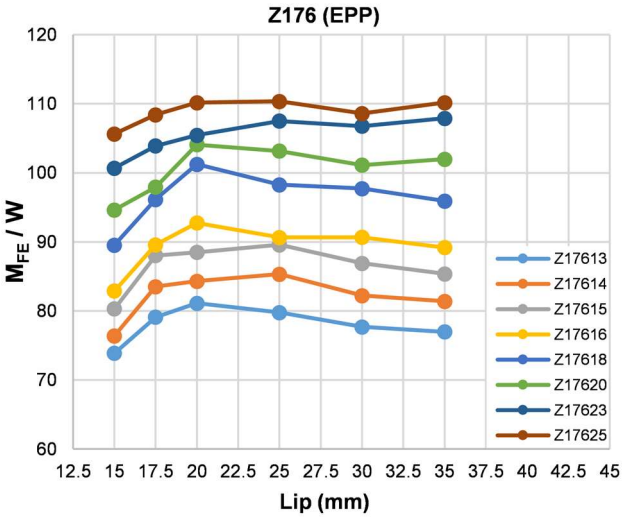
Z176 (EPP)
120
110
100
90
80
70
60
M_{FE} / W
12.5 15 17.5 20 22.5 25 27.5 30 32.5 35 37.5 40 42.5 45
Lip (mm)
Z17613
Z17614
Z17615
Z17616
Z17618
Z17620
Z17623
Z17625

(d)

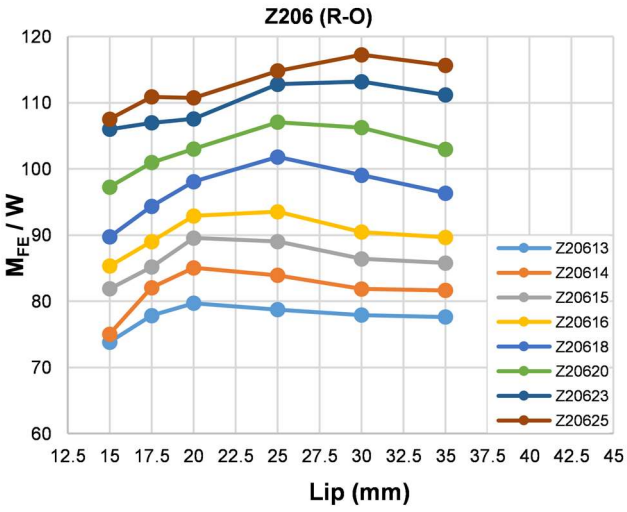
Z206 (R-O)
120
110
100
90
80
70
60
M_{FE} / W
12.5 15 17.5 20 22.5 25 27.5 30 32.5 35 37.5 40 42.5 45
Lip (mm)
Z20613
Z20614
Z20615
Z20616
Z20618
Z20620
Z20623
Z20625

(e)

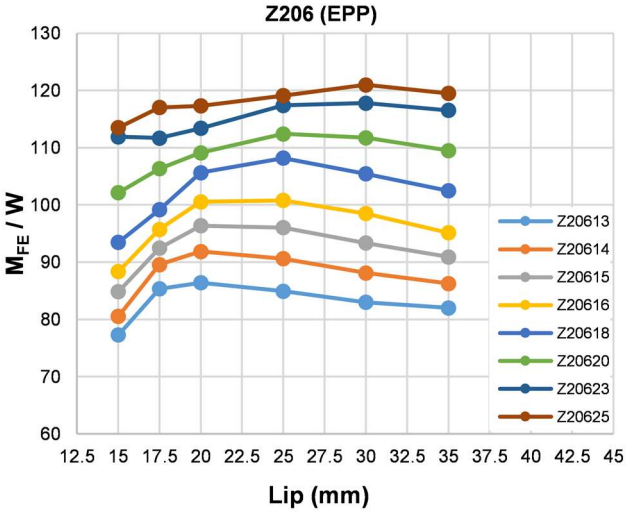
Z206 (EPP)
130
120
110
100
90
80
70
60
M_{FE} / W
12.5 15 17.5 20 22.5 25 27.5 30 32.5 35 37.5 40 42.5 45
Lip (mm)
Z20613
Z20614
Z20615
Z20616
Z20618
Z20620
Z20623
Z20625

(f)

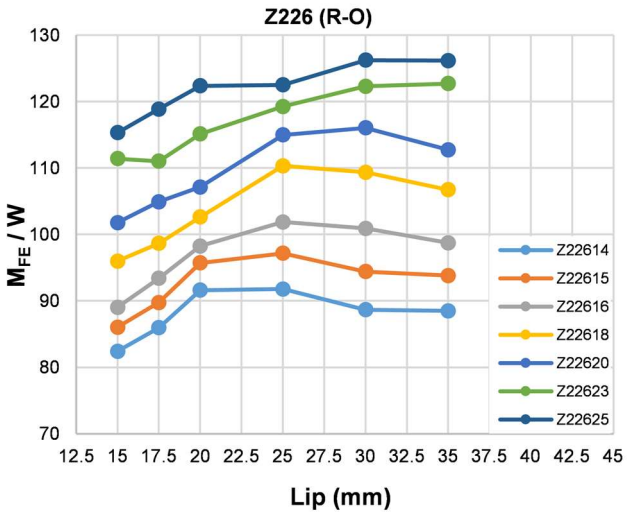
Z226 (R-O)
M_{FE} / W
Lip (mm)
Z22614
Z22615
Z22616
Z22618
Z22620
Z22623
Z22625

(g)

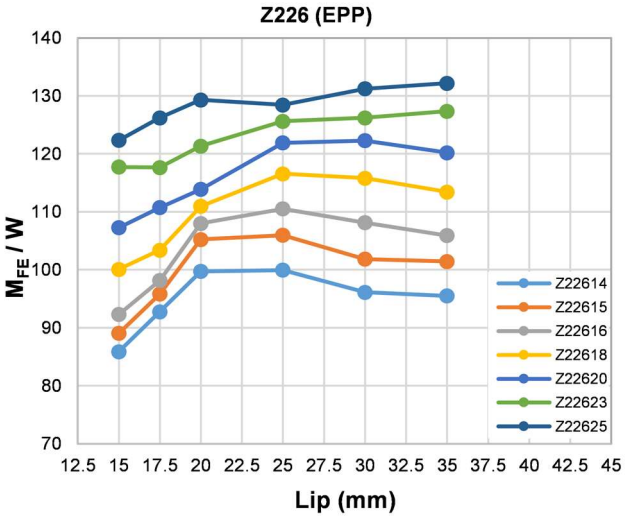
Z226 (EPP)
M_{FE} / W
Lip (mm)
Z22614
Z22615
Z22616
Z22618
Z22620
Z22623
Z22625

(h)

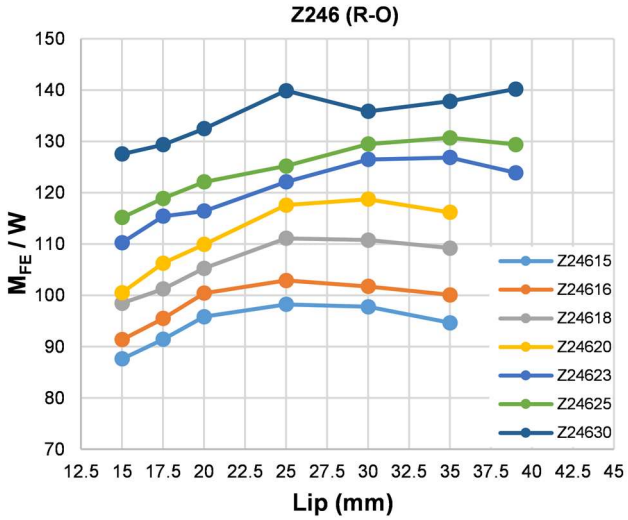
Z246 (R-O)
M_{FE} / W
Lip (mm)
Z24615
Z24616
Z24618
Z24620
Z24623
Z24625
Z24630

(i)

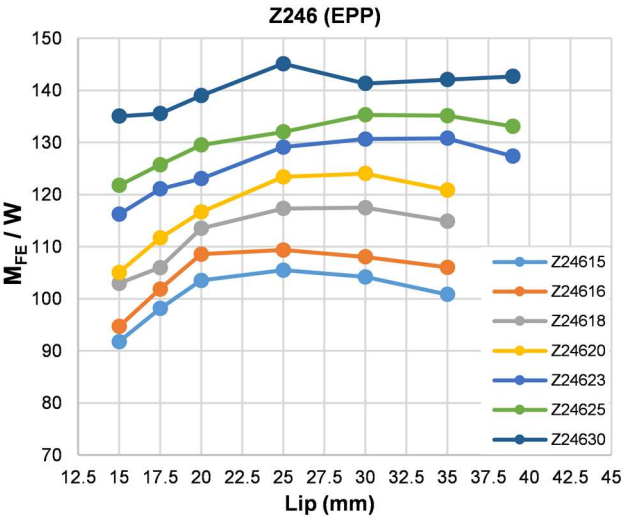
Z246 (EPP)
M_{FE} / W
Lip (mm)
Z24615
Z24616
Z24618
Z24620
Z24623
Z24625
Z24630

(j)

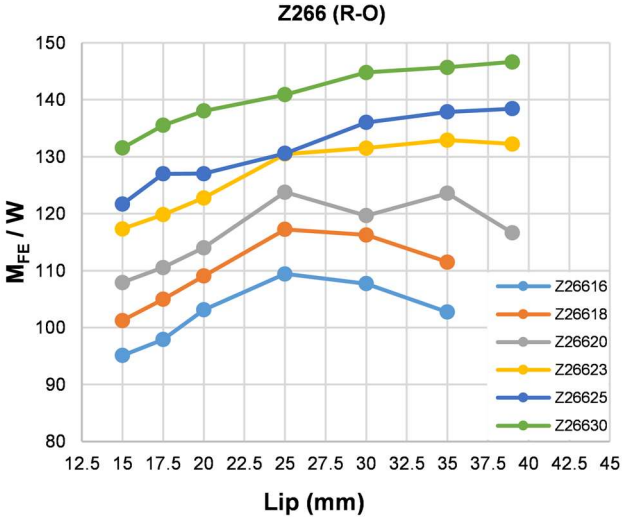
Z266 (R-O)
M_{FE} / W
Lip (mm)
Z26616
Z26618
Z26620
Z26623
Z26625
Z26630

(k)

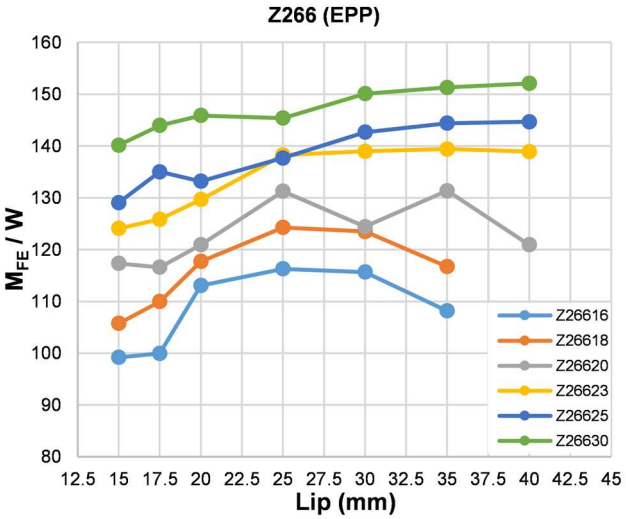
Z266 (EPP)
M_{FE} / W
Lip (mm)
Z26616
Z26618
Z26620
Z26623
Z26625
Z26630

(l)

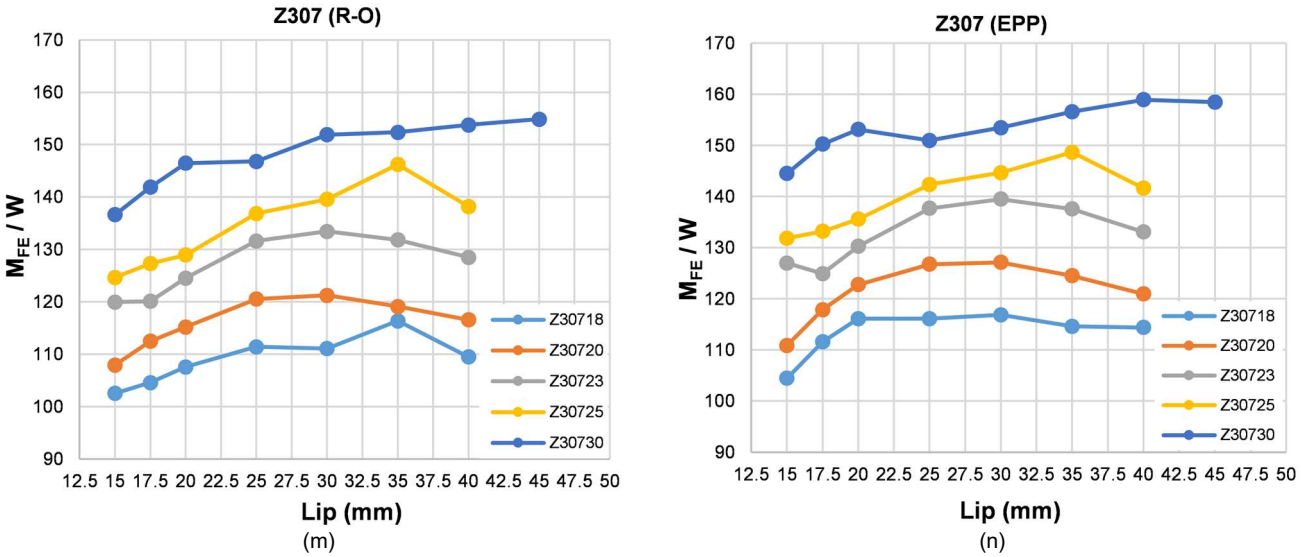

Fig. 11. Effect of lip size on moment-to-weight ratio.

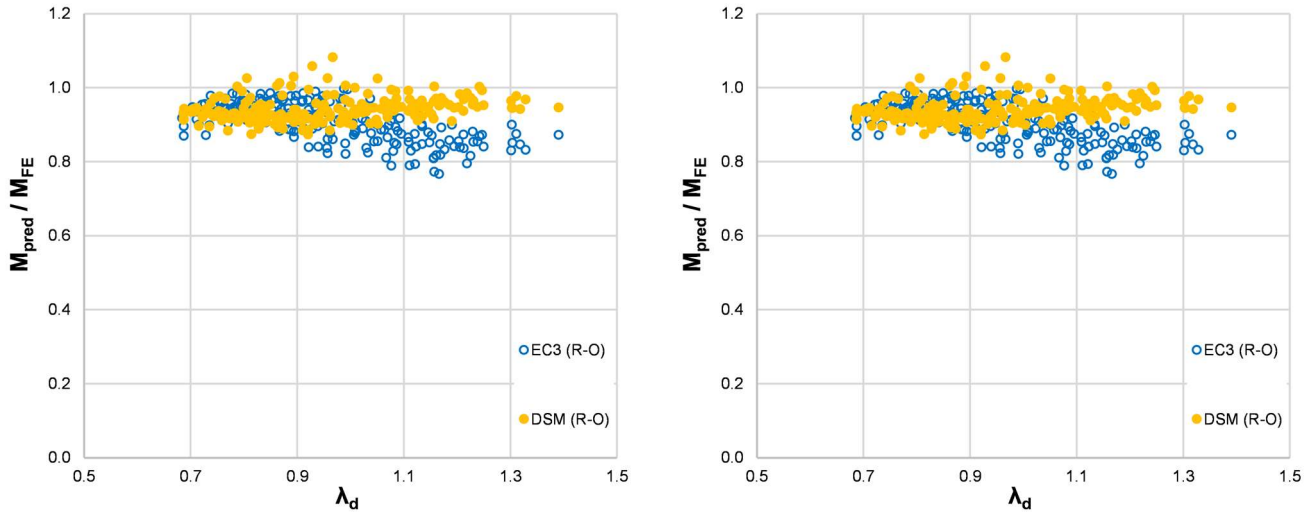

Fig. 12. Comparison of the EN 1993-1-3 [10] and DSM [8] moment resistance predictions against numerical results.

Table 1: Amplitudes considered for initial geometric imperfections.

	Local imperfection	Distortional imperfection
a	0.31 t	0.75 t
b	0.54 t	1.14 t
c	$0.8 * (h/200)$	$0.3 * t * (\sigma_{0.2}/\sigma_{crd})^{0.5}$

Table 2: Various modelling approaches for structural details.

Modelling approach	Computational Cost	Complexity
Model i): effect of struts and cladding modelled as boundary conditions	Low	Low
Model ii): struts and cladding explicitly modelled	High (necessitates modelling of contact, convergence issues)	High (necessitates modelling of contact)
Model iii): struts modelled as boundary conditions, cladding modelled explicitly	High	High (necessitates modelling of contact)
Model iv): struts explicitly modelled, cladding modelled as boundary condition	Low (additional degrees of freedom)	Moderate (strut details affect analysis-optimization not valid for other strut details)

Table 3: Effect of modelling approach on the accuracy of the predictions.

Specimen	M_{FE} / M_T i)	M_{FE} / M_T ii)	M_{FE} / M_T iii)	M_{FE} / M_T iv)
Z14613	0.95	0.97	0.96	0.97
Z14620	1.02	0.99	0.94	1.02
Z17613	0.97	0.96	0.99	0.97
Z17625	1.01	1.01	0.98	1.01
Z20620	1.08	1.10	1.08	1.08
Z24615	1.14	1.09	1.04	1.07
Z24620	1.04	1.04	1.04	1.04
Z30718	0.94	1.02	1.00	1.02
Average	1.02	1.02	1.00	1.02
COV	0.06	0.05	0.05	0.04

Table 4: Effect of initial geometric imperfections on predicted moment resistance.

Case	1			2			5			6		
Section	M_{FE}/M_T **a**	M_{FE}/M_T **b**	M_{FE}/M_T **c**	M_{FE}/M_T **a**	M_{FE}/M_T **b**	M_{FE}/M_T **c**	M_{FE}/M_T **a**	M_{FE}/M_T **b**	M_{FE}/M_T **c**	M_{FE}/M_T **a**	M_{FE}/M_T **b**	M_{FE}/M_T **c**
Z14613	0.98	0.93	0.96	0.97	0.92	0.95	1.01	0.96	0.98	1.00	0.96	0.98
Z14620	1.01	1.00	1.02	1.01	1.00	1.02	1.01	1.01	1.02	1.01	1.01	1.02
Z17613	0.99	0.95	0.97	0.98	0.94	0.97	1.01	0.99	0.99	1.00	0.97	0.99
Z17625	0.98	0.97	1.01	0.98	0.97	1.01	0.99	0.98	1.01	0.99	0.98	1.01
Z20620	1.07	1.04	1.08	1.07	1.04	1.08	1.09	1.06	1.11	1.09	1.05	1.09
Z24615	1.12	1.10	1.14	1.13	1.11	1.07	1.14	1.11	1.15	1.15	1.13	1.09
Z24620	1.03	0.99	1.04	1.04	1.01	1.01	1.05	1.02	1.05	1.05	1.03	1.03
Z30718	1.01	1.00	0.95	1.03	1.02	0.94	0.95	1.01	0.94	1.04	1.03	0.96
Average	1.02	1.00	1.02	1.03	1.00	1.01	1.03	1.02	1.03	1.04	1.02	1.02
COV	0.049	0.053	0.064	0.054	0.060	0.050	0.058	0.049	0.066	0.053	0.054	0.046

Table 5 Summary of geometric configurations and material models used in parametric studies

Section	h (mm)	b (mm)	t (mm)	d (mm)	Material	
Z146	145	62.5	1.3, 1.4, 1.5, 1.6, 1.8, 2	15, 17.5, 20, 25, 30, 35	$E = 200$ GPa $f_y = 450$ MPa	$E = 200$ GPa $\sigma_{0.2} = 450$MPa $\sigma_{1.0} = 455$MPa $n = 11$ $n_{0.2,1.0} = 1.5$
Z176	175	62.5	1.3, 1.4, 1.5, 1.6, 1.8, 2, 2.3, 2.5			
Z206	200	62.5	1.3,1.4, 1.5,1.6, 1.8, 2, 2.3, 2.5			
Z226	225	62.5	1.4, 1.5, 1.6, 1.8, 2, 2.3, 2.5			
Z246	245	62.5	1.5, 1.6, 1.8, 2, 2.3, 2.5, 3			
Z266	265	62.5	1.6, 1.8, 2, 2.3, 2.5, 3			
Z307	300	75	1.8, 2, 2.3, 2.5, 3			

Table 6 Normalised M_{FE}/W mean values for various lip depths and materials

Section	R-O					EPP				
	15/20	**17.5/20**	**25/20**	**30/20**	**35/20**	**15/20**	**17.5/20**	**25/20**	**30/20**	**35/20**
Z146	0.96	0.99	1.00	1.01	***1.04***	0.95	0.99	1.00	1.02	***1.05***
Z176	0.94	0.97	***1.01***	0.99	0.98	0.92	0.97	***1.00***	0.98	0.97
Z206	0.93	0.97	***1.02***	1.00	0.99	0.91	0.97	***1.01***	0.99	0.97
Z226	0.93	0.96	***1.03***	1.03	1.02	0.90	0.94	***1.03***	1.02	1.01
Z246	0.93	0.97	1.04	***1.05***	1.04	0.92	0.96	***1.03***	1.03	1.02
Z266	0.94	0.97	1.06	***1.06***	1.05	0.94	0.96	1.04	***1.05***	1.04
Z307	0.95	0.97	1.04	1.06	***1.07***	0.94	0.97	1.03	***1.04***	1.04

Table 7. Mean values of M_{pred}/M_{FE} ratio for EN 1993-1-3/5 [16,17] (EC3) and the DSM [18]

	R-O		EPP	
Section	**EC3**	**DSM**	**EC3**	**DSM**
Z146	0.90	0.97	0.84	0.92
Z176	0.88	0.96	0.84	0.90
Z206	0.88	0.96	0.83	0.90
Z226	0.88	0.94	0.82	0.88
Z246	0.90	0.94	0.86	0.89
Z266	0.92	0.93	0.87	0.88
Z307	0.93	0.96	0.89	0.92
Overall mean	0.90	0.95	0.85	0.90
COV	0.06	0.04	0.07	0.04